

# Motion and coalescence of sessile drops driven by substrate wetting gradient and external flow

Majid Ahmadiouydarab<sup>1</sup> and James J. Feng<sup>1,2,†</sup>

<sup>1</sup>Department of Chemical and Biological Engineering, University of British Columbia,  
Vancouver, BC V6T 1Z3, Canada

<sup>2</sup>Department of Mathematics, University of British Columbia, Vancouver, BC V6T 1Z2, Canada

(Received 20 March 2013; revised 29 January 2014; accepted 5 March 2014)

We report two-dimensional simulations of drop dynamics on a substrate subject to a wetting gradient and an external pressure gradient along the substrate. A phase-field formulation is used to represent the drop interface, and the moving contact line is modelled by Cahn–Hilliard diffusion. The Navier–Stokes–Cahn–Hilliard equations are solved by finite elements on an adaptively refined unstructured grid. For a single drop and a pair of drops, we consider three scenarios of drop motion driven by the wetting gradient only, by the external flow only, and by a combination of the two. Both the capillary force and the hydrodynamic drag depend strongly on the shape of the drop. Since the drop adapts its shape to the local wetting angles and to the external flow on a finite time scale, hysteresis is a prominent feature of the drop dynamics under opposing forces. For each wetting gradient, there is a narrow range of the magnitude of the external flow within which a single drop can achieve a stationary state. The equilibrium drop shape and position depend on its initial shape and the history of forcing. For a pair of drops, the wetting gradient or external flow alone tends to produce catch-up and coalescence. The flow-driven coalescence arises from a viscous shielding effect that relies on the asymmetric shape of the trailing drop once it is deformed by flow. This mechanism operates at zero Reynolds number, but is much enhanced by inertia. With the two forces opposing each other, the external flow favours separation while the wetting gradient favours coalescence. The outcome depends on their competition.

**Key words:** contact lines, drops, breakup/coalescence

---

## 1. Introduction

The present study has been motivated by efforts to optimize the air–water transport through the gas diffusion layer in hydrogen fuel cells. This is a porous medium through which air flows to the reaction site while water, a product of the reaction, is discharged (Wang 2004; Nam *et al.* 2009). Water vapour condenses in the hydrophobic pores, and small droplets are believed to coalesce and then be driven out partly by wetting gradients, typically produced by hydrophobic coatings or a microporous layer. Meanwhile, the incoming air creates a counterflow, which tends to drive the water droplets in the opposite direction (Gurau & Mann 2009). How do sessile drops move

† Email address for correspondence: [jfeng@chbe.ubc.ca](mailto:jfeng@chbe.ubc.ca)

and coalesce on a substrate subjected to a wetting gradient and an external flow? This is the question that we set out to investigate.

Considerable work has been done on drop motion driven by wetting gradients. Early theoretical models (Greenspan 1978; Brochard 1989) balance the driving force, the net capillary force due to the asymmetry in contact angles, against the viscous friction to predict the drop velocity. These models typically neglect drop deformation and assume the shape of a spherical cap for the drop, its footprint being a circle of radius  $R$ . Then they posit a driving force proportional to  $SR^2$  and a viscous friction proportional to  $UR$ , where  $S = d(\cos \theta)/dx$  is the wetting gradient,  $\theta$  being the local contact angle, and  $U$  is the drop velocity. Thus,  $U$  turns out to be proportional to  $SR$ . The models differ mostly in the treatment of the contact-line singularity and determination of the viscous friction. One can estimate the friction locally from Tanner's law (Brochard 1989), or calculate it using the wedge-flow solution of Cox (1986) or a lubrication solution (Subramanian, Moumen & McLaughlin 2005). In the end, the difference amounts to a different prefactor. As an example, Subramanian *et al.* (2005) derived the following approximate formula for vanishing contact angles and a linear  $d\theta/dx$ :

$$U = \frac{\sigma R \theta^2}{6\eta_d \ln(2l_s)} \left( \frac{d\theta}{dx} \right), \quad (1.1)$$

where  $\sigma$  is the surface tension,  $\eta_d$  is the drop viscosity and  $l_s$  is the slip length. Recently, Xu & Qian (2012) presented phase-field simulations of the motion of a sessile drop on a wetting gradient. Their approach is more sophisticated than prior theoretical models, with the drop deformation properly calculated and the contact-line singularity regularized by liquid–vapour phase change. However, the results are qualitatively the same.

Experimentally, the idea of moving droplets by wetting gradients was demonstrated by Chaudhury & Whitesides (1992). Ito *et al.* (2007) reported that  $U$  increases nonlinearly with  $S$  on a number of substrates. The more recent data of Daniel *et al.* (2004) show a linear dependence. Moumen, Subramanian & McLaughlin (2006) measured drop motion on a nonlinear wetting gradient, and their experimental data confirmed theoretical predictions based on balancing the driving force and the friction force. The last two studies have also considered the effects of contact-angle hysteresis. Based on this brief summary of theoretical, numerical and experimental work, the motion of a single droplet on a non-uniformly wetting substrate is well understood.

Drop motion driven by an external flow has been investigated by several groups (Schleizer & Bonnecaze 1999; Dimitrakopoulos & Higdon 2001; Kang, Zhang & Chen 2005; Zhang, Miksis & Bankoff 2006; Ding, Gilani & Spelt 2010; Dupont & Legendre 2010; Mognetti, Kusumaatmaja & Yeomans 2010), but only on a substrate with uniform wettability. Herde *et al.* (2012) studied the equilibrium configuration and motion of a drop driven by a body force on substrates with a sinusoidal wettability pattern. This seems to have come closest to the situation of interest here, except that our drop will be driven by an external viscous flow. Considerable work has been done on drop coalescence on homogeneous substrates (Ristenpart *et al.* 2006; Narhe, Beysens & Pomeau 2008; Hernández-Sánchez *et al.* 2012; Karpitschka & Riegler 2012), with a focus on the asymptotic behaviour of the liquid bridge that forms between the drops. However, little can be found in the literature on drop–drop interaction on wetting gradients. The most relevant studies dealt with coalescence between a drop moving on a wetting gradient and a stationary one resting on an adjoining substrate of uniform wettability (Lai, Hsu & Yang 2010; Wang *et al.* 2010).

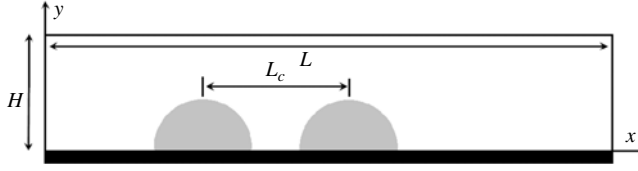


FIGURE 1. Schematic of the initial configuration for 2D planar computations. The drops have an effective diameter  $D$ , and the geometry is specified by the length ratios  $\alpha = L/D$ ,  $\beta = H/D$ , and for two drops,  $\gamma = L_c/D$ .

Besides, to our knowledge, there have been no studies of drop coalescence driven by external flow.

This work is an effort towards filling these gaps in knowledge. Using a diffuse-interface model and finite elements on an adaptive unstructured grid, we carry out systematic planar two-dimensional (2D) simulations of drop motion and coalescence on a substrate. For a single drop and a pair of drops, we consider three scenarios in which the drop motion is driven by (a) a wetting gradient, (b) an external flow of the surrounding fluid parallel to the substrate, and (c) a combination of the two. In particular, we investigate the competition between the two driving forces, and how they determine drop–drop coalescence. For the simple case of a single drop on a wetting gradient, we also report a three-dimensional (3D) simulation that helps to benchmark the numerical parameters used in 2D simulations.

## 2. Problem set-up and methodology

We examine two related phenomena: the motion of a single sessile drop, and the coalescence of a pair of sessile drops. Most of the simulations to be reported are in a 2D planar geometry, with a rectangular computational domain of length  $L$  and height  $H$  (figure 1). If the contact angle varies monotonically along the substrate, no drop shape will be at equilibrium. As soon as the drop makes contact with the substrate, it adjusts to the local contact angles, deforms and starts to move. For consistency, we have used an initial drop shape of a semicircle in most of the 2D simulations. The only exception is figure 8, which examines the effect of the initial drop shape. From the area of the drop  $A$ , we define its effective diameter  $D = \sqrt{8A/\pi}$ , which will be used as the characteristic length throughout the paper. Three domain sizes have been used. For single-drop simulations,  $\alpha = L/D = 6.67$  and  $\beta = H/D = 0.834$ . The two-drop simulations have a somewhat larger domain to accommodate the merged drop:  $\alpha = 7.88$  and  $\beta = 0.985$ . The initial drop separation  $\gamma = L_c/D$  will be given for individual runs. Numerical experiments show that the domain is long enough so that  $\alpha$  has negligible effect on the drop motion. The domain height  $\beta$  is chosen to be of order one so as to model a small pore; its value affects drop motion driven by an external flow, but not that driven by wetting gradients on the substrate. Finally, to compare with experiments in § 3.1, we have adopted the experimental geometry with  $\alpha = 8.11$  and  $\beta = 0.845$ . In the 3D simulation, the drop is initially a hemispherical cap.

The problems to be computed involve the deformation and movement of the interface, a three-phase contact line, and non-uniform wettability. We have chosen a diffuse-interface formulation with the Cahn–Hilliard model for the purpose. The Cahn–Hilliard diffusion regularizes the interfacial jump as well as the contact-line singularity, and provides a convenient means for interface capturing. The Navier–Stokes–Cahn–Hilliard system is solved using a finite-element method on an unstructured and

adaptively refined grid. The theoretical model and numerical algorithm have been described and validated at length in previous publications (Yue *et al.* 2006b; Zhou *et al.* 2010; Ahmadlouydarab, Liu & Feng 2011; Gao & Feng 2011a,b; Mehrabian & Feng 2011; Yue & Feng 2011a). For brevity, we will only list the governing equations and boundary conditions and mention a few features of the numerical method.

A phase-field variable  $\phi$  is introduced such that  $\phi = 1$  in one fluid and  $\phi = -1$  in the other. The two-phase flow in the computational domain is described by the Navier–Stokes and Cahn–Hilliard equations:

$$\nabla \cdot \mathbf{u} = 0, \quad (2.1)$$

$$\rho \left( \frac{\partial \mathbf{u}}{\partial t} + \mathbf{u} \cdot \nabla \mathbf{u} \right) = -\nabla p + \nabla \cdot [\eta(\nabla \mathbf{u} + \nabla \mathbf{u}^T)] + \mu \nabla \phi + \mathbf{B}, \quad (2.2)$$

$$\frac{\partial \phi}{\partial t} + \mathbf{u} \cdot \nabla \phi = m \nabla^2 \mu, \quad (2.3)$$

where  $m$  is the Cahn–Hilliard mobility,  $\mu = \lambda[-\nabla^2 \phi + \phi(\phi^2 - 1)/\epsilon^2]$  is the chemical potential and  $\mu \nabla \phi$  is the diffuse-interface representation of the interfacial tension. The two parameters  $\lambda$  and  $\epsilon$  are, respectively, the interfacial energy density and the capillary width of the interface, their ratio giving the interfacial tension in the limit of sharp interfaces (Yue *et al.* 2006b),  $\sigma = (2\sqrt{2}/3)(\lambda/\epsilon)$ ; and  $\mathbf{B}$  is a constant body force that is used in the present problem to impose a pressure gradient on the fluids and produce the external flow. A physical pressure drop  $\Delta P$  over the length of the domain  $L$  is realized through the body force  $\mathbf{B}$  having the magnitude  $\Delta P/L$ . The viscosity  $\eta$  and density  $\rho$  are averages between the two fluids weighted by their volume fractions  $(1 + \phi)/2$  and  $(1 - \phi)/2$ . For droplets of submillimetre diameters, the Bond number is much below unity. Thus we have neglected gravity. Similarly, for the operating conditions that motivated this work, the Reynolds number is typically  $Re = O(10^{-2})$  (Koido, Furusawa & Moriyama 2008), and we have neglected inertia for most of the simulations.

On the solid substrate, the following boundary conditions are used:

$$\mathbf{u} = 0, \quad (2.4)$$

$$\mathbf{n} \cdot \nabla \mu = 0, \quad (2.5)$$

$$\lambda \mathbf{n} \cdot \nabla \phi + f'_w(\phi) = 0, \quad (2.6)$$

where  $\mathbf{n}$  is the normal vector pointing into the wall, and  $f'_w(\phi) = -\sigma \cos \theta (\phi(3 - \phi^2)/4)$  is a wall energy (Yue, Zhou & Feng 2010; Yue & Feng 2011b). Equation (2.4) imposes no slip on the substrate, and contact-line motion is realized via Cahn–Hilliard diffusion. As a consequence, the ‘contact-line velocity’ is extracted not from the velocity field  $\mathbf{u}$ , but from the movement of the point of contact, i.e. the point where the interface  $\phi = 0$  intersects the substrate. Equation (2.5) implies no penetration of the fluid components into the wall. Equation (2.6) is a natural boundary condition that follows from the variation of the wall energy, and specifies the local contact angle  $\theta$  (Yue *et al.* 2010). A wetting gradient is represented by the spatial variation of the local contact angle through this boundary condition.

We impose stress-free boundary conditions on the top, the left and the right sides of the domain. To simulate an external flow driven by a horizontal pressure gradient, we impose the body force  $\mathbf{B}$  on both fluids. Thus a Poiseuille velocity profile develops at the entry and exit of the domain, as they are sufficiently far from the drops. We

---

	$\alpha$	$\beta$	$Cn$	$\Lambda$	$M$
One-drop simulations	6.67	0.834	$6.7 \times 10^{-3}$	$8.33 \times 10^{-3}$	50
Two-drop simulations	7.88	0.985	$6.7 \times 10^{-3}$	$8.33 \times 10^{-3}$	50

---

TABLE 1. Parameter values used in most of the simulations reported in this paper. A few computations have tested different values, and these will be noted individually.

---

use the Galerkin finite-element method on a triangular grid, with an implicit time-marching scheme and Newton iterations at each time step. The grids near the fluid interface are adaptively refined and coarsened as the interface moves. The algorithm has been validated previously using 2D and 3D drop-motion problems as benchmarks (Yue *et al.* 2006b; Zhou *et al.* 2010).

In presenting results, we use the effective drop diameter  $D$  as the characteristic length, and the capillary time  $t_c = \eta_d D / \sigma$  as the characteristic time,  $\eta_d$  being the drop viscosity. The dimensionless parameters of the problem include the length ratios indicated in figure 1, the drop-to-medium viscosity ratio  $M = \eta_d / \eta_m$  and the density ratio  $\rho_d / \rho_m$ . As mentioned above, most of the simulations are inertialess; the density ratio is relevant only to one set of inertial results in §4.2. Besides, the wetting gradient  $S = d(\cos \theta) / dx$  is made dimensionless as  $G = DS$ , and the maximum contact angle at the hydrophobic end of the substrate is specified as  $\theta_m$ . When external flow is present, we have an ‘effective Bond number’  $F = BD^2 / \sigma$  that indicates the strength of the external flow relative to the surface tension. Note that  $F$  is defined using the body force  $B$  driving the flow; it has nothing to do with gravity, which is neglected in this study.

Besides these, the Cahn–Hilliard model introduces two mesoscopic dimensionless parameters: the Cahn number  $Cn = \epsilon / D$ , and the diffusion parameter  $\Lambda = l_d / D$ . The former is the ratio between the interfacial thickness and the macroscopic length, while the latter is that between the *diffusion length*  $l_d = (\eta_d \eta_m)^{1/4} m^{1/2}$  and  $D$ . These must be chosen judiciously; and  $Cn$  should be small enough so that the sharp-interface limit is approached (Yue *et al.* 2006b; Zhou *et al.* 2010). For 2D drop motion on a substrate, we have found that reducing  $Cn$  from  $2 \times 10^{-2}$  to  $6.7 \times 10^{-3}$  causes at most a 0.5 % difference in the drop position throughout the simulation. Hence all subsequent 2D results are computed using  $Cn = 6.7 \times 10^{-3}$ . As  $l_d$  is the counterpart of the *slip length*  $l_s$  commonly used in sharp-interface models (Yue *et al.* 2010; Yue & Feng 2011b),  $\Lambda$  represents the strength of Cahn–Hilliard diffusion in moving the contact line, and is closely related to the contact-line speed. Thus, it should in principle be determined by fitting an experimental datum for the specific fluids and substrate material (Yue & Feng 2011a,b). The selection of the  $\Lambda$  value will be discussed next in §3.1. The parameter values used in most of the simulations are summarized in table 1.

We should note that the sharp-interface limit of diffuse-interface models for moving contact lines is still under active investigation (Wang & Wang 2007; Yue *et al.* 2010). Alternative choices of the mobility  $m$  have been explored, for example by Magaletti *et al.* (2013) and Sibley, Nold & Kalliadasis (2013a). For moving contact lines in a one-component liquid–vapour system, Sibley *et al.* (2013b) have analysed the asymptotic limit of the diffuse-interface model at the contact line. A similar analysis has been presented by Sibley *et al.* (2013a) for binary-fluid Cahn–Hilliard and Allen–Cahn systems. Although the present study does not focus on the sharp-interface limit itself, it is important to recognize that ours is one of several possible approaches to it.

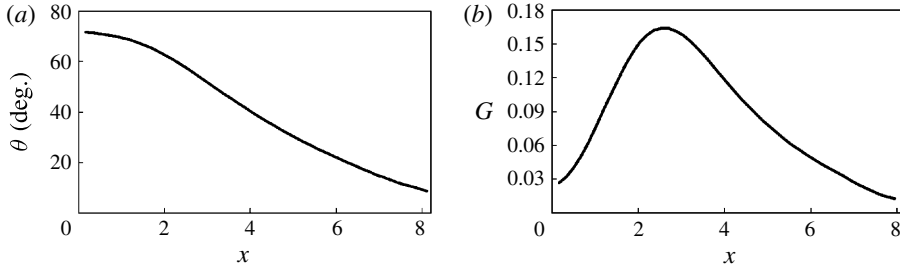


FIGURE 2. Experimental conditions of Moumen *et al.* (2006) used to benchmark our simulation: (a) contact-angle profile along the solid substrate; (b) profile of the dimensionless wettability gradient  $G$ .

### 3. Results: the motion of a single sessile drop

#### 3.1. Single drop driven by wettability gradient

This subsection has two objectives. The first is to use the prior theoretical and experimental results (Subramanian *et al.* 2005; Moumen *et al.* 2006) to benchmark our simulations and to determine the parameter  $\Lambda$ , and the second is to examine the motion of a single sessile drop driven by a uniform wetting gradient.

Moumen *et al.* (2006) conducted an experiment on the motion of sessile drops on a substrate bearing a prescribed profile of the wetting angle, which is reproduced in figure 2 along with the dimensionless wetting gradient  $G$ . They compared their experimental results with the prediction of slip-based theoretical models of Subramanian *et al.* (2005) applied to the wetting gradient of figure 2. We will simulate the drop motion under the same wetting gradient. Yue *et al.* (2010) have previously shown that our diffusion length  $l_d$  is related to the slip length  $l_s$  by  $l_s \approx 2.5l_d$ . The same relationship has been confirmed for the sliding drops in the current study. This is the basis for evaluating our  $l_d$  and  $\Lambda$ .

Figure 3 compares our 2D simulations using two values of  $\Lambda$  with the model predictions of Subramanian *et al.* (2005) based on Cox's wedge-flow approximation. Inertia is neglected in all four calculations. The drop centre  $x_c$  is the midpoint between the two contact lines, scaled by the effective drop diameter  $D$ . The instantaneous drop velocity  $U$ , taken to be the average between the velocity of the two contact lines, is non-dimensionalized into a capillary number  $Ca = \eta_d U / \sigma$ . Our diffusion lengths are matched to their slip lengths by  $l_s = 2.5l_d$ . Thus our computations at  $\Lambda = 2.14 \times 10^{-3}$  and  $8.33 \times 10^{-3}$  correspond, respectively, to slip lengths of  $l_s/D = 5.35 \times 10^{-3}$  and  $2.83 \times 10^{-2}$ . The drop velocity roughly mirrors the profile of the wetting gradient  $G$  (figure 2b); the drop accelerates first, and then decelerates as it spreads out on the increasingly hydrophilic substrate. As expected, the drop moves faster at the larger  $\Lambda$  value or slip length. The slip-model predictions are somewhat lower than our numerical results. This quantitative discrepancy is not surprising since the model is based on various simplifications and approximations, e.g. the assumption of a spherical cap and the wedge-flow approximation. Moreover, the Cox solution was based on matched asymptotics over an inner, an intermediate and an outer region, and such a structure was not maintained in the model of Subramanian *et al.* (2005). Although this model is not a perfect benchmark for our calculation, it appears to be the closest that can be found in the literature. The comparison in figure 3 offers a basis on which to choose our numerical diffusion length.



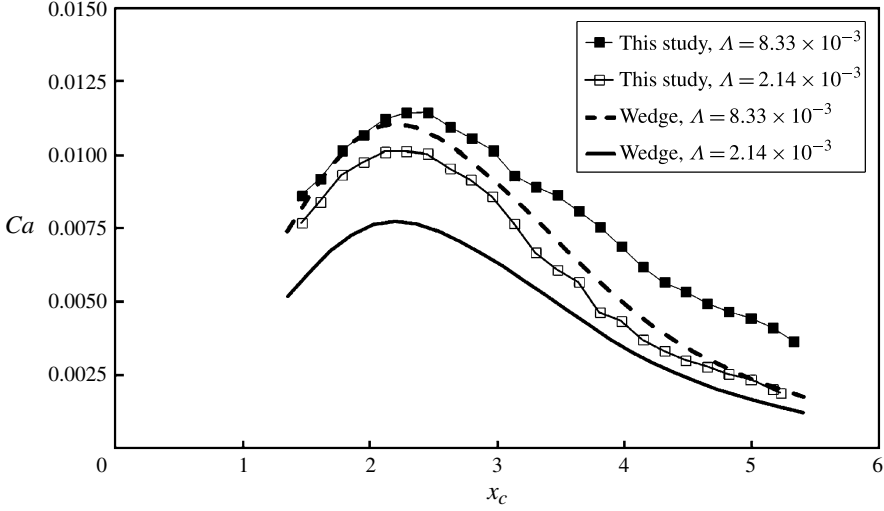


FIGURE 3. Comparison of the droplet centre velocity, non-dimensionalized into a capillary number, between our 2D computations and the wedge-flow model predictions of Subramanian *et al.* (2005). For each  $\Lambda$  value, a slip length  $l_s = 2.5l_d = 2.5\Lambda D$  is used in the theoretical model. The geometric parameters  $\alpha = 8.11$  and  $\beta = 0.845$  correspond to the experimental geometry.

It remains to be determined whether the  $\Lambda$  values tested above are realistic. As noted before (Fermigier & Jenffer 1991; Yue & Feng 2011a,b), the slip lengths for real materials are usually in the nanometre range, much below the typical resolution of continuum computations. Thus, previous computations using sharp-interface and diffuse-interface models alike have adopted computable slip lengths  $l_s/D = O(10^{-2})$  (Schleizer & Bonnecaze 1999; Dupont & Legendre 2010), comparable to those in figure 3. To illustrate this limitation, we have done a 3D simulation and compared it with the experimental result of Moumen *et al.* (2006) (figure 4). The 3D computational domain has a width of  $W = 2D$ , and the drop is located in the centre plane. The front half of the box is computed with symmetry conditions imposed on the centre plane that cuts the drop in half. At  $\Lambda = 6.76 \times 10^{-3}$ , close to the minimum diffusion length that we can readily compute in three dimensions, our phase-field simulation overpredicts the drop velocity by a factor of roughly 5. The wedge-flow model overpredicts by a smaller amount at the corresponding slip length. Moumen *et al.* (2006) also tested the model at a much smaller slip length,  $l_s = 0.5$  nm, corresponding to  $\Lambda = 1.35 \times 10^{-7}$ . Now the prediction is within a factor of 2 of the measurement. Thus, it is clear that we will have to settle for a larger computable  $\Lambda$  value as others have done. To achieve quantitative agreement with experiments, Yue & Feng (2011a,b) introduced wall-energy relaxation in the Cahn–Hilliard model to compensate for using an unrealistically large diffusion length. However, such relaxation allows the dynamic contact angle to deviate from the static one, and this may complicate the representation of the wetting gradient. In this study we will not strive to match a specific experiment, and thus have used  $\Lambda = 8.33 \times 10^{-3}$  for all the 2D simulations presented hereafter. This needs to be kept in mind when interpreting the numerical results quantitatively.

We now turn to the more general question of the behaviour of a sessile drop on a *constant* wetting gradient  $G$ . As the drop experiences viscous friction on the

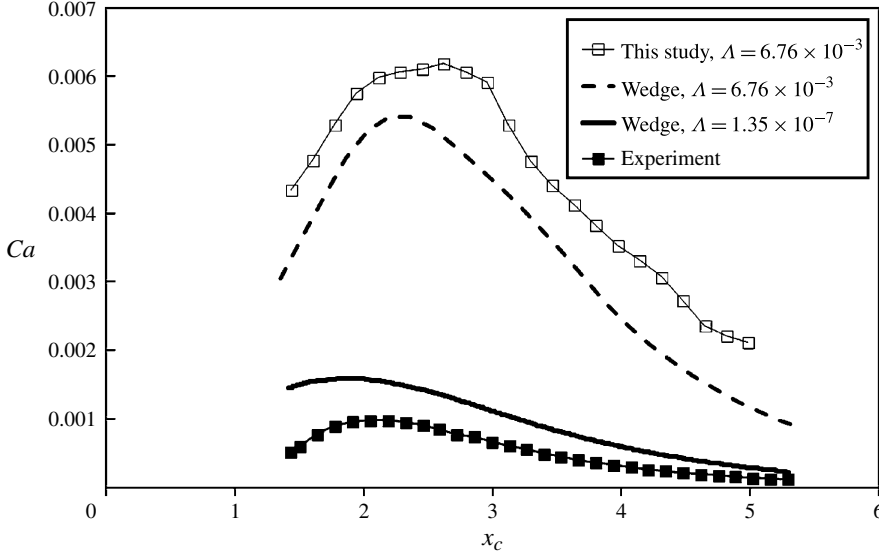


FIGURE 4. Comparison of the drop centre velocity among our 3D computation, experimental measurement and theoretical predictions of the wedge-flow model (Moumen *et al.* 2006). Our computation is based on  $Cn = 2.03 \times 10^{-2}$  and  $\Lambda = 6.76 \times 10^{-3}$ , and one of the wedge-flow predictions is at the corresponding slip length. A much smaller  $l_s/D = O(10^{-7})$  is needed to predict the experimental data. The geometric parameters  $\alpha = 8.11$  and  $\beta = 0.845$  correspond to the experimental geometry.

substrate as well as on its upper surface, its motion turns out to be sensitive to the viscosity of both the drop and the surrounding fluid. Figure 5 shows the evolution of the instantaneous drop velocity for four different  $M$  values as the drop traverses the substrate with a fixed  $G$ . The capillary number  $Ca$  exhibits a gentle acceleration for  $M = 1$  but a deceleration for large  $M$ . As inertia has been neglected, the drop velocity is determined by the balance between two forces: the driving force due to the differing contact angles at the leading and trailing edges, and the hydrodynamic drag. The latter consists of an internal friction between the drop and the substrate, and an external drag due to the surrounding medium. As the drop moves downstream into more hydrophilic areas, the driving force increases with the lengthening footprint of the drop. The change in the drag, on the other hand, depends on  $M$ . For  $M = 1$ , the medium is as viscous as the drop and the external drag is significant. As the drop spreads, the internal friction increases not only because the footprint of the drop lengthens, but also because the decreasing height induces greater shear rates inside. In the meantime, the external drag declines with the height of the spreading drop. The balance between the driving force and the total drag is such that the drop sees a slight acceleration in this case. For larger  $M$ , achieved by reducing the outer viscosity, the external drag becomes insignificant and the drop moves faster. Now the increasing internal friction overwhelms the increasing driving force to produce the gentle deceleration. Note also that the effect of  $M$  diminishes for larger  $M$ ; the medium viscosity becomes negligible. For all subsequent results, we have used a fixed  $M = 50$  to approximate the viscosity ratio between water and air at room temperature. For such an  $M$ , the external drag can be neglected in analysing the results.

To explore the effect of the wetting gradient  $G$ , we track the average velocity of the drop from the inception of its motion at  $x_c = 2.08$  till  $x_c = 4.17$ , and plot the



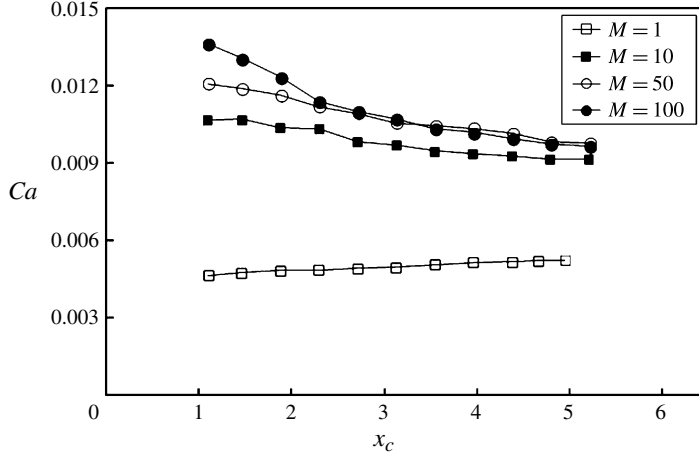


FIGURE 5. Instantaneous velocity of the sessile drop on a substrate with a constant wettability gradient for four values of the viscosity ratio  $M = \eta_a/\eta_m = 1, 10, 50$  and  $100$ ; for  $G = 0.144$ ,  $\theta_m = 92.3^\circ$ .

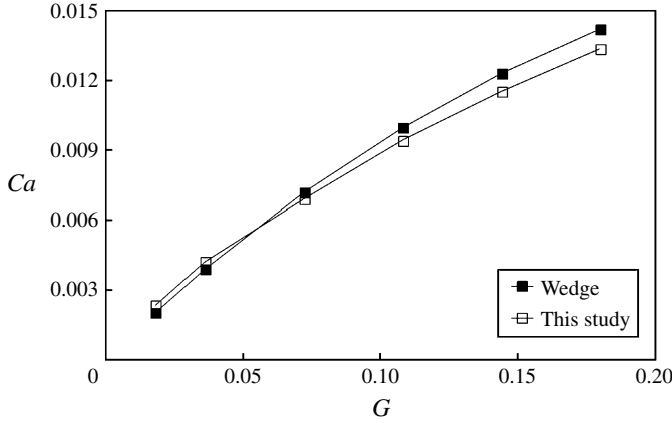


FIGURE 6. The average velocity of the drop measured between  $x_c = 2.08$  and  $x_c = 4.17$  as a function of the dimensionless wettability gradient  $G$ . Our computation is compared with the wedge-flow model of Moumen *et al.* (2006).

capillary number based on this average velocity as a function of the wetting gradient  $G$  (figure 6). As expected, the drop velocity increases with  $G$ . The driving force, due to the differing contact angles at the two contact lines, is proportional to  $G$ . As the drop moves downstream, however, its changing shape affects the viscous friction in a nonlinear fashion. Thus, the  $Ca \sim G$  relationship is not strictly linear. This is supported by the wedge-flow approximation, whose prediction is also plotted for comparison.

### 3.2. Single drop driven by external flow

The motion of a sessile drop driven by an external flow has been studied by several groups before, for example Schleizer & Bonnecaze (1999) and Ding *et al.* (2010), and

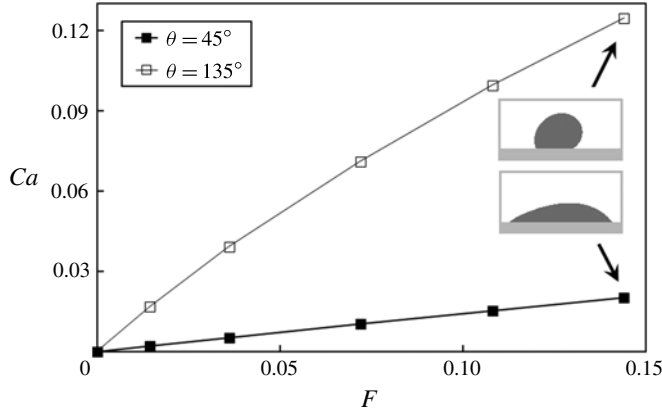


FIGURE 7. Dependence of the steady-state drop velocity, in terms of the capillary number  $Ca$ , on the driving force  $F$  for two contact angles. The insets indicate the degree of drop deformation at the largest  $F$  value in each case.

the physics is more or less well understood. The objective of this brief subsection is to reprise the basic features of the motion as they are relevant to the more complex scenarios to be discussed later in the paper.

Consider a drop on an ideal substrate with a uniform contact angle  $\theta$ . In the absence of contact-angle hysteresis, such a drop moves with the slightest external forcing. We impose a constant body force on both the drop and the surrounding fluid; this is equivalent to applying a fixed pressure drop over the length of our computational domain. A shear flow develops and sweeps over the drop, which deforms and starts to move. In roughly  $10t_c$  both the external flow and the drop motion approach a steady state. Our geometric set-up of figure 1 is such that a parabolic velocity profile develops at the entry and the exit. Because of the additional dissipation incurred by the sessile drop, the steady-state centreline velocity is lower than that expected in a Poiseuille flow, which is  $u_m = BH^2/(2\eta_m)$  in dimensional form, and the deficit depends on the drop size and the contact angle.

The steady-state velocity of the drop, in terms of the capillary number  $Ca = \eta_d U / \sigma$ , is plotted in figure 7 against the dimensionless driving force  $F$  for two contact angles,  $\theta = 45^\circ$  and  $135^\circ$ . Note that an ‘external capillary number’ can be defined using the characteristic velocity  $u_m$  of the external flow, the medium viscosity  $\eta_m$  and the effective drop diameter  $D$ :  $Ca_m = \eta_m u_m / \sigma = \frac{1}{2} F \beta^2$ , which ranges from 0 to  $5.22 \times 10^{-2}$  for the  $F$  values in figure 7. In our inertialess flow, the drop velocity is determined by a balance between the driving force on the drop surface due to the external flow and the viscous friction on the substrate. The deformation of the drop, which is appreciable in the parameter range of figure 7 (see insets), should have introduced nonlinearity into the problem. Yet, surprisingly,  $Ca$  scales more or less linearly with the driving force  $F$ . A similar linear dependence has been reported in the literature (Schleizer & Bonnecaze 1999; Ding *et al.* 2010). Furthermore, the drop moves faster on a more hydrophobic substrate; it has a smaller footprint and is also taller, and thus experiences a larger driving force and a smaller friction. At higher flow rates and with inertia, the drop may become entrained by the flow and pinch off from the wall (Schleizer & Bonnecaze 1999; Kang *et al.* 2005), but such regimes are not directly relevant to the current study.

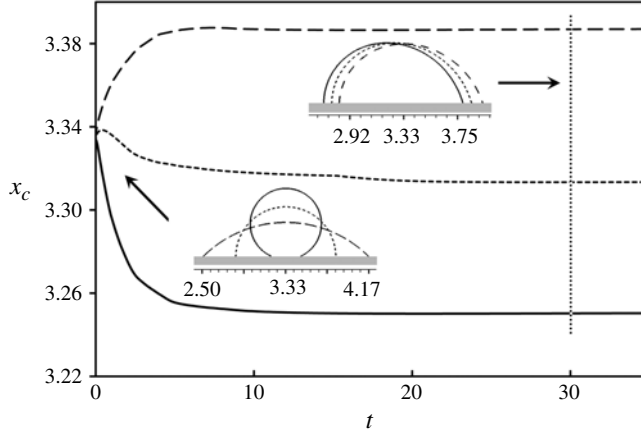


FIGURE 8. Trajectory of drops starting from three initial shapes with instantaneous contact angles of  $45^\circ$ ,  $90^\circ$  and  $135^\circ$ . The drop is initially centred at  $x_0 = 3.33$ . The constant wetting gradient, with  $G = 0.245$  and  $\theta_m = 130^\circ$ , drives the drop towards the right, while the external flow at  $F = 6.12 \times 10^{-2}$  goes to the left. The insets illustrate the initial and final shapes of the drop.

### 3.3. Competition between external flow and wetting gradient

If the external flow and the wetting gradient push the drop in the same direction, the two effects reinforce each other and the outcome is faster drop motion. If the two oppose each other, their competition can be quite subtle; the drop dynamics exhibits a sensitivity to initial conditions and forcing history, and is therefore hysteretic. This can perhaps be anticipated from the fact that both the capillary force and the external force depend intimately on the shape of the drop. For example, the drop's footprint on the substrate defines the magnitude of the capillary force, and its hump determines the hydrodynamic drag that the external flow exerts on it. In addition, the viscous friction depends on the shape of the drop as well. Thus, depending on the initial drop configuration and the flow history, the outcome of the competition may vary. Note that this hysteresis is unrelated to wetting angle hysteresis.

We have probed this hysteresis by numerical experiments. Figure 8 compares the trajectory of three drops starting from the centre of the domain (initial drop centre position at  $x_0 = 3.33$ ) with different initial shapes, the instantaneous contact angle being  $45^\circ$ ,  $90^\circ$  and  $135^\circ$ . The initially tallest drop experiences the greatest drag from the external flow, and starts to move downstream (to the left). As the contact lines adjust to the local wetting angles, however, the drop spreads out. Consequently, the hydrodynamic drag on the drop declines, while the wetting force increases. The two eventually reach a balance when the drop comes to rest at  $x_r = 3.25$ , having moved approximately 8.4% of its effective diameter  $D$ . Similarly, the initially most spread-out drop favours the wetting gradient and moves to the right (final position  $x_r = 3.39$ ), and the intermediate drop winds up at an intermediate position ( $x_r = 3.31$ ). If  $F$  and  $G$  are grossly mismatched, the drop may find no stationary state at all. This scenario will be examined shortly. We have also tested the dependence on the history of the control parameters, and confirmed that, depending on how  $F$  varies in time, the drop can be driven to different equilibrium positions and shapes even though the final  $F$  is the same.

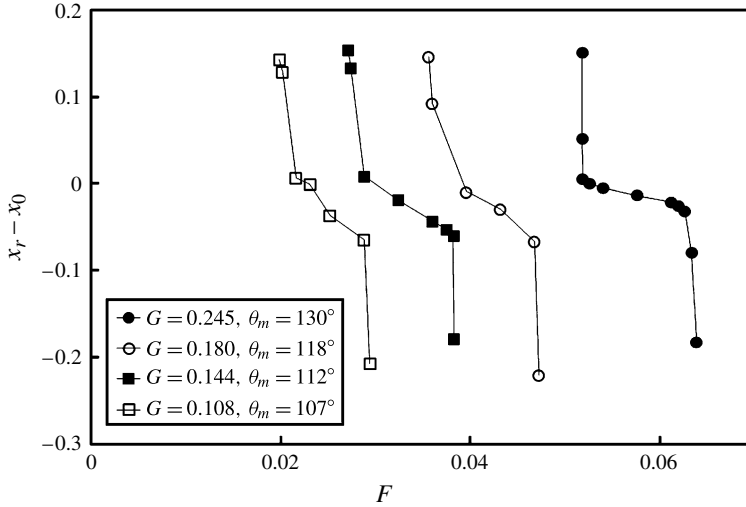


FIGURE 9. Final position for a single drop that has come to rest under the opposing actions of  $F$  and  $G$ . The y-axis shows the displacement of the drop centre scaled by the effective drop diameter. Initially the drop is centred at  $x_0 = 3.33$ .

This hysteretic behaviour, i.e. dependence on initial configuration and history of the control parameters, is rooted in the fact that it takes a finite time, of the order of the capillary time  $t_c$ , for the drop to adjust its shape. It is a fundamental feature of the  $F \sim G$  competition in the current flow set-up. Perhaps unfortunately, this implies that the quantitative results of the simulations, if not the qualitative trends, are specific to the initial conditions used. In the following, we will use a consistent initial condition to investigate the  $F \sim G$  competition, with the drop being a semicircle centred at  $x_0 = 3.33$ , the substrate bearing a constant  $G$  towards the right, and the external flow at a fixed  $F$  being turned on at  $t = 0$  in the opposite direction. When comparing such numerical results with experiments, one needs to beware of the initial conditions in the latter, and to keep the hysteretic effects in mind.

Starting from this initial condition, we simulate the motion of the drop at different combinations of  $(F, G)$  values. The final resting position of the drop centre,  $x_r$ , is plotted in figure 9 as a function of  $F$  for a series of  $G$  values. This figure paints a rather delicate picture about the  $F \sim G$  competition. For each  $G$  value, there is a narrow range of  $F$  within which a stationary state can be achieved. Within this range, the drop stops further to the hydrophilic area (larger  $x_r$ ) for larger  $G$  and smaller  $F$ , and to the hydrophobic area (smaller  $x_r$ ) for smaller  $G$  and larger  $F$ . The stationary drop assumes such a shape that the hydrodynamic and capillary forces balance each other. It is a fragile balance. For an  $F$  value outside the narrow range, the hydrodynamic force will never be balanced by the capillary force. The drop moves continually to the left or right, and no state of rest is achieved.

It is somewhat surprising that the drop attains a stationary state at all. One may imagine shifting the drop slightly to the left by external perturbation. Then the substrate becomes more hydrophobic and the drop is supposed to bulge upwards. This would reduce the capillary force and increase the hydrodynamic drag, and the drop would then continue to move to the left. This argument seems to suggest a linear instability of any resting position. What makes the rest state possible is again

the hysteretic nature of the system. After the imagined slight shift to the left, the drop shape does not immediately adapt to the local contact angle; that process takes a finite time of the order of the capillary time  $t_c$ . The ensuing change in drop shape and hence the hydrodynamic drag cannot be anticipated from the simple ‘equilibrium’ argument posed above. In fact, there is no equilibrium shape to which to relax on a wetting gradient. We have carried out further numerical experimentation on the delicate balance between  $F$  and  $G$ . Taking one of the curves in figure 9 corresponding to a fixed  $G$ , we vary  $F$  in small increments, each time after a new stationary position has been established. In this way, we have managed to reach a much wider range of equilibrium positions for a much wider  $F$  range than indicated in figure 9, where all stationary states have been reached from the same initial position under a fixed  $F$ . This confirms the central role of hysteresis in defining the stationary state for the drop.

It is instructive to note the similarity between the drop dynamics discussed above and that described by Herde *et al.* (2012). Their drop is driven by a body force, and the wetting gradient has a sinusoidal pattern with a period much smaller than the drop size. Thus, multiple equilibrium states can be predicted from the energetics. They have identified certain ranges of initial positions that will lead to a rest state. Those ranges narrow and eventually disappear with increasing driving force. Once in motion, the drop exhibits hysteresis and bistability much as our flow-driven drop. Despite the difference in the driving mechanism, the hysteresis has essentially the same origin in both cases. Herde *et al.* (2012) summarized it as such: ‘Hysteresis is ... because the moving droplet is never at its equilibrium shape for the given positions of the back and front contact points.’ The same holds for our drop.

## 4. Results: drop–drop coalescence

### 4.1. Coalescence driven by wettability gradient

On a substrate with a constant wetting gradient, the merging of two sessile drops can be anticipated from the motion of each drop alone. Figure 5 has shown that, in a low-viscosity medium ( $M \geq 10$ ), a single drop will decelerate as it moves into increasingly hydrophilic regions, thanks to the increasing viscous friction on the substrate. When two identical drops are placed on such a substrate with an initial separation, the one initially on the more hydrophobic area will catch up with the other, and coalesce with it. Figure 10 demonstrates such a process. In fact, this merging can hardly be called ‘interaction’, as it arises mostly from the behaviour of single drops at different positions on the substrate. Since the surrounding fluid has low viscosity, the two drops move more or less independently of each other. As one may expect, the time for catch-up increases with initial separation and decreases with the wetting gradient  $G$ .

### 4.2. Coalescence driven by external flow

Now we place two drops on a substrate of uniform wetting angle  $\theta = 105^\circ$ , at an initial separation of  $\gamma = 1.035$ . After turning on an external flow driven by  $F = 0.309$ , the two drops both start to move downstream (figure 11). Based on the characteristic velocity of the external flow  $u_m$  and the medium viscosity  $\eta_m$ , the external capillary number for each drop is  $Ca_m = 0.150$ , large enough to produce considerable drop deformation. In time, the trailing drop catches up with the leader, and the two merge into one. The coalescence of two interfaces is a subtle process in the phase-field model that involves Cahn–Hilliard diffusion and short-range attractive forces (Yue *et al.* 2005; Yue, Zhou & Feng 2006a). Note that the point of initial contact is a small

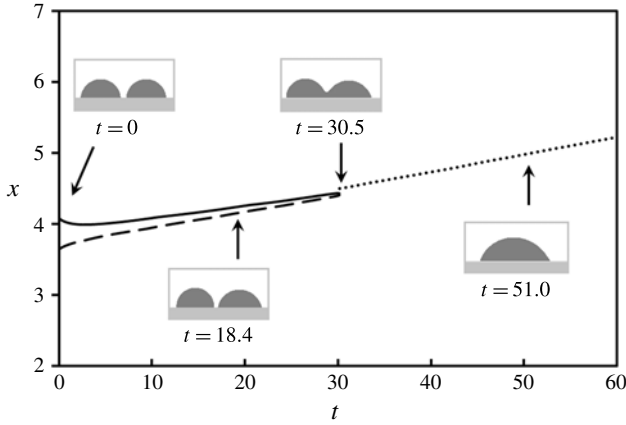


FIGURE 10. Coalescence of two identical drops on a substrate with a constant wetting gradient  $G=0.244$  and maximum contact angle  $\theta_m=164^\circ$ . The drops are initially centred at  $x=3.30$  and  $4.44$  ( $\gamma=1.14$ ), and the solid and dashed curves indicate the trajectories of the rear contact line of the leading drop and the front contact line of the trailing drop. After merging at  $t=30$ , the centre of the new drop moves according to the dotted line.

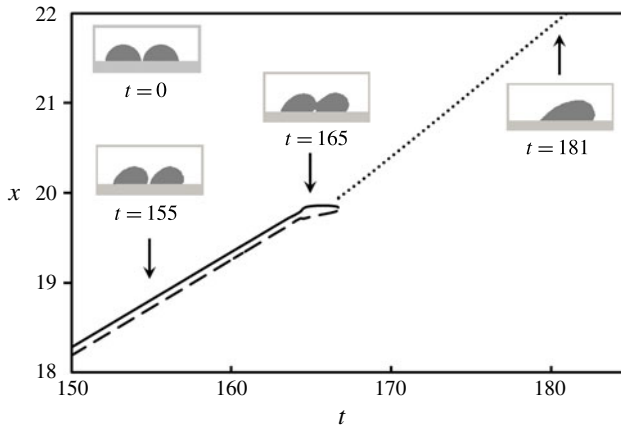


FIGURE 11. Flow-driven coalescence of two identical drops on a substrate with contact angle  $\theta = 105^\circ$ ;  $F = 0.309$  points towards the right. The drops are initially centred at  $x=1.46$  and  $2.48$  ( $\gamma=1.035$ ), and the curves indicate drop positions in the same way as in figure 10. Coalescence starts at  $t=164$ . To magnify the view of the trajectories near the point of coalescence, we have omitted the initial period until  $t=150$ .

distance above the substrate. Thus a small air bubble is trapped in the merged drop ( $t=165$ ), a common phenomenon when two curved surfaces collide (Yue *et al.* 2005). Interfacial diffusion can lead to the disappearance of the entrapped bubble, as occurs here between  $t=165$  and  $t=167.5$  (not shown). The reader may consult Yue, Zhou & Feng (2007) for detailed discussions of this process. The merged drop moves with a steady-state velocity  $U$  that corresponds to a capillary number  $Ca = \eta_d U / \sigma = 0.147$ . Note that the catch-up takes rather a long time, and the drops have moved through the length of the domain a few times. To accommodate the long simulation in this case, we have adopted periodic boundary conditions at the two ends of the domain.



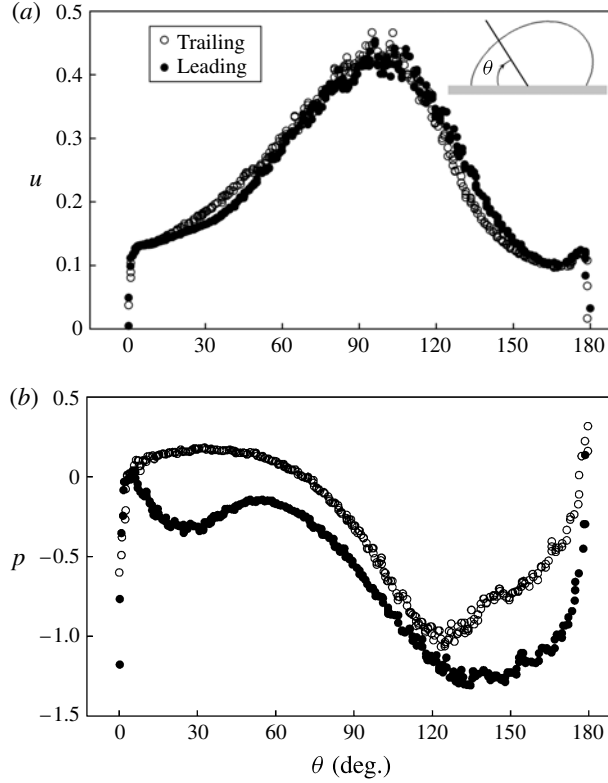


FIGURE 12. Comparison of (a) the  $x$  component of the velocity and (b) the pressure distribution on two drops at a dimensionless time  $t=123$ . The velocity and pressure values are taken along the contour of  $\phi=0.9$ , just outside the interface, and are plotted against the polar angle  $\theta$  measured from the midpoint between the two contact lines. Velocity and pressure are made dimensionless by  $\sigma/\eta_d$  and  $\sigma/D$ , respectively.

The coalescence implies that, despite the absence of inertia, the trailing drop experiences a greater hydrodynamic drag than the leading one. To investigate this, we have analysed the velocity, pressure and stress distributions around the two drops. As the drops start to move, both deform, with the top tilting downstream (figure 11,  $t=155$ ). This is similar to the shape of a single pinned bubble predicted by asymptotic theories (Feng & Basaran 1994; Sugiyama & Sbragaglia 2008). Such bubble deformation creates a relatively narrow gap between the drops, where the velocity of the surrounding fluid is suppressed by viscosity. This is demonstrated in figure 12(a) by comparing profiles of  $u$ , the  $x$  component of the velocity, around the two drops. At the contact lines,  $u$  exhibits very large gradients within an effective ‘slip layer’ produced by Cahn–Hilliard diffusion (Yue *et al.* 2010). However, the feature of interest here is that the leading drop experiences a lower velocity on its upstream side than the trailing drop. This can be thought of as a viscous shielding effect due to the asymmetric shape of the trailing drop. In Stokes flow around an object with fore–aft symmetry, no such shielding is expected. A direct consequence of the shielding is a lower pressure on the upstream side of the leading drop (figure 12b). Note that the pressure also varies sharply within the slip layer. Since this layer contributes little to the overall hydrodynamic drag, we have matched the two pressure profiles at a

small distance of  $4.16\epsilon$  off the substrate at the upstream contact line. This distance is roughly the interfacial thickness (Yue *et al.* 2004), and corresponds to a polar angle of  $3.4^\circ$  off the substrate. The pressure being set to zero at this point, the rest of the profile shows clearly that the shielded drop experiences much reduced dynamic pressure on its upstream side. This explains the greater driving force on the trailing drop, and the eventual merging of the two. We have also analysed the viscous shear and normal stresses around the drops. The pressure contributes roughly 85 % of the total drag, and is therefore the dominant factor. At the instant analysed in figure 12, the pressure force on the trailing drop is 35 % greater than that on the leading one, and the total drag is 32 % greater. Numerical experiments show that, if the two drops are initially farther apart, the shielding effect will be weaker, and the flow-driven coalescence will take longer. In principle, the drops will always interact hydrodynamically because of the elliptic nature of the Stokes flow.

Recall that our study was motivated by drop motion in hydrogen fuel cells, and the typical operating conditions correspond to negligible inertia. But since inertia is known to affect hydrodynamic interaction among particles and drops (Feng, Hu & Joseph 1994; Olapade, Singh & Sarkar 2009), we carried out a set of simulations to explore the effect of finite Reynolds numbers. At  $Re = \rho_m u_m D / \eta_m = 13$ , with a drop-to-medium density ratio of 100 and a viscosity ratio of 50, the merging of the two drops happens much more quickly. Under the same conditions as in figure 11, the two drops first touch at a dimensionless time of 17.0, down from 164 without inertia. Evidently, the shielding effect is much enhanced by inertia. For the rest of the results to be presented, inertia will again be omitted.

#### 4.3. Competition between external flow and wetting gradient

Let us consider the interaction of two sessile drops when a wetting gradient  $G$  and an external flow  $F$  are both at work. As in § 3.3, we expect the drop dynamics to exhibit hysteresis, i.e. sensitivity to initial conditions and forcing history. For simplicity and brevity, we will not explore hysteresis at length in this subsection, and will use the same initial drop shape (semicircle) and constant  $F$  and  $G$  forcing in the following.

The situation is simpler if  $F$  and  $G$  are co-current, i.e. oriented in the same direction. Both  $F$  and  $G$  promote catch-up in this case, and it is no surprise that the catch-up time decreases monotonically when either driving force is increased. Figure 13 demonstrates this effect for an increasing  $F$ . Note that  $F$  exerts a larger force on the trailing drop not only because of viscous shielding, as discussed in figure 12, but also because the trailing drop sits in a more hydrophobic area, and thus presents a taller hump to the external flow. On the other hand, the catch-up distance  $d$ , defined as the distance travelled by the centre of the trailing drop up to the instant of coalescence, shows a *non-monotonic* dependence on  $F$  (figure 13). A larger  $F$  produces faster motion on both drops. For the  $G$  value used, increasing  $F$  beyond roughly 0.05 will cause the catch-up distance to increase as the gain in drop velocity more than compensates for the loss in catch-up time. This non-monotonicity may have already been present for the  $F$ -only scenario of figure 11. Since coalescence happens slowly when driven solely by  $F$ , we have not carried out the numerous long runs required to confirm this. We have also tested the effect of varying  $G$  at a fixed  $F$ . For increasing  $G$ , both the catch-time and the catch-up distance decrease monotonically. This is because the leading drop spreads out more rapidly downstream, and thus decelerates more quickly.

Now we consider the counter-current situation, with the external flow towards the left and the wetting gradient driving the drop towards the right. In this case,

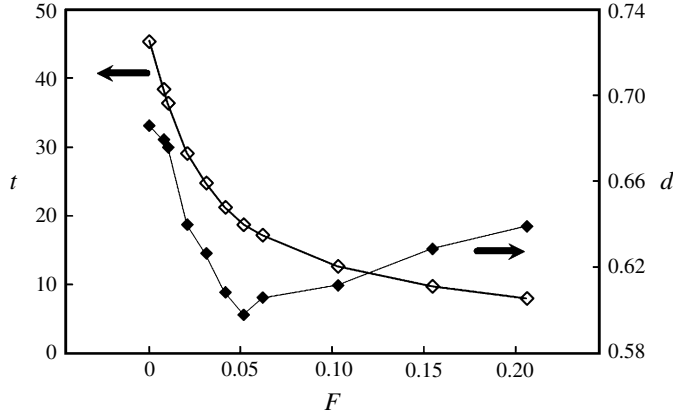


FIGURE 13. Drop coalescence under co-current  $F$  and  $G$ : the catch-up time  $t$  and catch-up distance  $d$  as functions of  $F$  for a fixed  $G=0.183$  and  $\theta_m=136^\circ$ . Initially the drops are centred at  $x=3.30$  and  $4.44$ , with initial separation  $\gamma=1.14$ . The catch-up distance  $d$  is defined as the distance travelled by the centre of the trailing drop up to the time of coalescence.

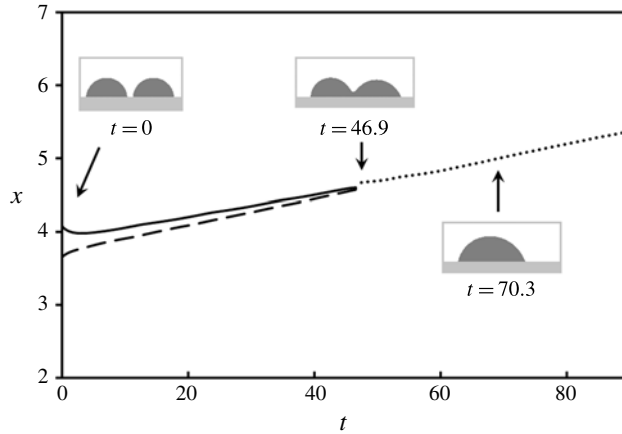


FIGURE 14. Drop coalescence under opposing effects of the external flow (towards the left) and the wetting gradient (towards the right); for  $G=0.244$ ,  $\theta_m=164^\circ$  and  $F=0.01$ . The initial configuration is identical to that of figure 10, and the curves have the same meanings. Coalescence occurs at  $t=46$ .

the presence of the wetting gradient fundamentally modifies the shielding effect, and the  $F \sim G$  competition cannot be anticipated from the effect of each alone. Keeping  $G$  fixed and increasing  $F$  gradually, we have observed two distinct scenarios, with coalescence or separation of the drops. Coalescence occurs for a sufficiently small  $F$  such that it weakens but does not overwhelm the  $G$ -driven catch-up and coalescence discussed in § 4.1. An example is shown in figure 14 for  $G=0.244$ ,  $\theta_m=164^\circ$  and  $F=0.01$ . Both drops are driven by  $G$  to move towards the right. Since the leading drop sits on a more hydrophilic surface, it spreads out more and consequently experiences less hydrodynamic drag from the external flow. Thus, the trailing drop (on the left) receives a greater drag due to the external flow, which

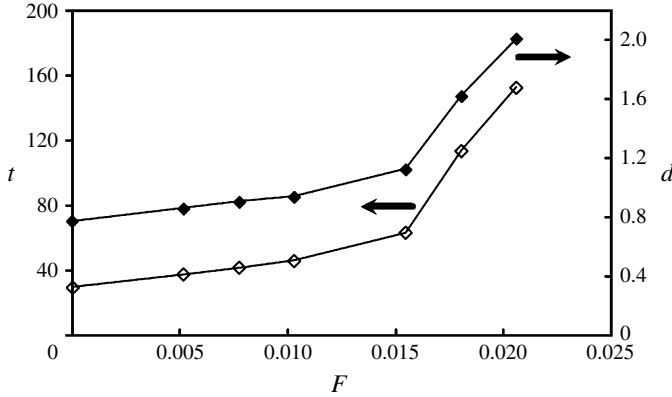


FIGURE 15. The catch-up time  $t$  and catch-up distance  $d$  both increase with  $F$ , other conditions being the same as in figure 14.

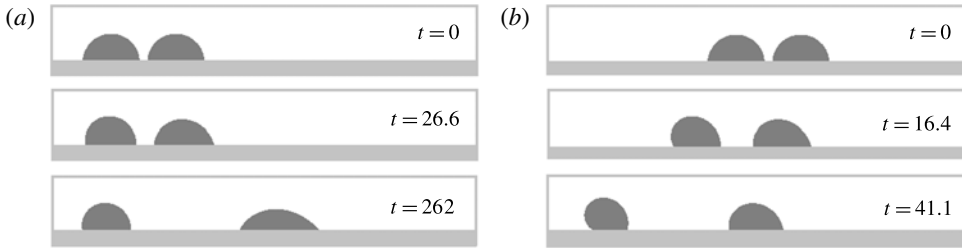


FIGURE 16. Drop separation under opposing effects of the external flow (towards the left) and the wetting gradient (towards the right); for  $G = 0.244$ ,  $\theta_m = 164^\circ$ . The initial configuration is identical to that of figure 10. (a) At  $F = 0.051$ , the right drop continues to the right but the left one moves to the left. (b) At  $F = 0.154$ , both drops move to the left while separating from each other.

hinders its motion and delays the catch-up and coalescence. The catch-up time and distance both increase monotonically with  $F$  in this scenario (figure 15).

Since  $F$  exerts a larger drag on the left drop, a sufficiently large  $F$  will prevent coalescence altogether. This is the second scenario, drop separation. Depending on the relative strength of  $F$  and  $G$ , each of the two drops may continue to move to the right, come to rest, or reverse course and move to the left, according to the single-drop dynamics of figure 9. In principle, therefore, one may envision several sub-scenarios of non-coalescence. Figure 16 illustrates two of those. At the moderately large  $F = 0.051$  (figure 16a), the drag on the left drop overpowers the  $G$ -induced driving force. It stops, and then reverses direction and moves slowly to the left. In the meantime, the right drop continues to move to the right, and the two separate. For the even larger  $F = 0.154$  (figure 16b), the hydrodynamic drag on both drops is able to overcome the wetting force. Thus, both drops are driven towards the left. Since the right drop spreads out more, it receives a smaller driving force from  $F$ , a greater resistance from  $G$ , as well as a larger viscous friction on the substrate. Thus it lags behind the left drop, and the two separate in time.

In the above we have largely anticipated the separation and coalescence between drops from the movement of each alone. Their hydrodynamic interaction plays a

secondary role and does not affect the qualitative features of the process. This forms an interesting contrast to § 4.2, where coalescence is entirely due to viscous shielding.

## 5. Conclusion

Using a diffuse-interface formalism, we have carried out a numerical investigation of the motion and coalescence of sessile drops driven by a wettability gradient, an external flow along the substrate, or both. Even with one of the two forcing agents at work, the drops exhibit interesting dynamics. When the two are set against each other, their competition can produce subtle and sometimes unexpected effects on the dynamics of sessile drops, including hysteresis and either coalescence or separation of the drops. The new findings of the study, within the parameter ranges investigated, are summarized as follows:

- (a) A single sessile drop on a constant wetting gradient decelerates in its motion provided that the viscosity of the surrounding medium is much lower than that of the drop. This is due to the increasing viscous friction on the drop as it moves into more hydrophilic areas.
- (b) When the wetting gradient is opposed by an external flow, the motion of a single drop exhibits a strong dependence on the initial condition and the history of forcing. The hysteresis arises because both the wetting force and the hydrodynamic drag depend strongly on the drop shape, and the drop shape adapts to local contact angles and external flows not instantaneously but on a finite time scale.
- (c) Two identical drops driven by a constant wetting gradient will coalesce into one. This is a direct result of the deceleration of each drop, with the leading one suffering a greater reduction in speed.
- (d) Two identical drops driven by an external flow will coalesce, thanks to a viscous shielding effect associated with the asymmetric shape of the upstream drop. This occurs even at zero Reynolds number, but is greatly enhanced by inertia.
- (e) When the wetting gradient is opposed by an external flow, two drops may coalesce or separate, depending on the relative strength of the two forcing agents. Coalescence is favoured by a stronger wettability gradient, and separation by a stronger external flow.

These results may have practical implications for microfluidic devices and micro-fabrication processes that rely on the manipulation of droplets. For example, the sensitivity to initial conditions and forcing history may lead to new strategies for controlling drop motion, coalescence and deposition. By balancing the effects of external flow and substrate wettability, one may design gas diffusion layers for optimal air–water transport in hydrogen fuel cells, the engineering application that has served as our initial motivation.

In the meantime, we point out several limitations of the present work that should be kept in mind when interpreting the numerical results quantitatively. First, most of the simulations are in two dimensions. Comparisons with our own limited 3D simulations and with 3D experiments show qualitative agreement but quantitative differences. One may well expect, for instance, the viscous shielding effect to be attenuated in three dimensions relative to its 2D counterpart. Second, we do not yet have a satisfactory physical model for the moving contact line, and its numerical simulation invariably requires additional *ad hoc* input. In our case, it is the Cahn–Hilliard diffusivity, which produces a diffusion length that is the counterpart of the slip length in sharp-interface

models. Third, we have not strived for a comprehensive description of the hysteretic effect. After testing a few scenarios to demonstrate the sensitivity of drop motion to initial conditions and forcing history, we have limited subsequent simulations to a uniform initial condition for ease of analysis. Potentially there may exist other, more exotic, regimes of drop dynamics that can be realized through different initial conditions and forcing history. Finally, we have ignored surfactants and Marangoni flows in our simulations and discussions, which often play important roles in reality. For example, Karpitschka & Riegler (2012) presented interesting observations and analysis on the merging of dissimilar but miscible sessile drops, where temporary non-coalescence may be maintained by a surface tension gradient and Marangoni flow. Such scenarios remain to be explored in future work.

### Acknowledgement

We thank Pengtao Yue, Peng Gao and Giovanni Ghigliotti for their assistance with the numerical algorithm and the computations, and Simon Liu and Xiaotao Bi for their comments on the manuscript. The study was supported by NSERC, the Canada Research Chair program, and the Canada Foundation for Innovation.

### REFERENCES

- AHMADLOUYDARAB, M., LIU, Z.-S. & FENG, J. J. 2011 Interfacial flows in corrugated microchannels: flow regims, transitions and hysteresis. *Intl J. Multiphase Flow* **37**, 1266–1276.
- BROCHARD, F. 1989 Motions of droplets on the solid surfaces induced by chemical or thermal gradients. *Langmuir* **5**, 432–438.
- CHAUDHURY, M. K. & WHITESIDES, G. M. 1992 How to make water run uphill. *Science* **256**, 1539–1541.
- COX, R. G. 1986 The dynamics of the spreading of liquids on a solid surface. Part 1. Viscous flow. *J. Fluid Mech.* **168**, 169–194.
- DANIEL, S., SIRCAR, S., GLIEM, J. & CHAUDHURY, M. K. 2004 Ratcheting motion of liquid drops on gradient surfaces. *Langmuir* **20**, 4085–4092.
- DIMITRAKOPOULOS, P. & HIGDON, J. J. L. 2001 On the displacement of three-dimensional fluid droplets adhering to a plane wall in viscous pressure-driven flows. *J. Fluid Mech.* **435**, 327–350.
- DING, H., GILANI, M. N. H. & SPELT, P. D. M. 2010 Sliding, pinch-off and detachment of a droplet on a wall in shear flow. *J. Fluid Mech.* **644**, 217–244.
- DUPONT, J.-B. & LEGENDRE, D. 2010 Numerical simulation of static and sliding drop with contact angle hysteresis. *J. Comput. Phys.* **229**, 2453–2478.
- FENG, J. Q. & BASARAN, O. A. 1994 Shear flow over a translationally symmetric cylindrical bubble pinned on a slot in a plane wall. *J. Fluid Mech.* **275**, 351–378.
- FENG, J., HU, H. H. & JOSEPH, D. D. 1994 Direct simulation of initial value problems for the motion of solid bodies in a Newtonian fluid. Part 1. Sedimentation. *J. Fluid Mech.* **261**, 95–134.
- FERMIGIER, M. & JENFFER, P. 1991 An experimental investigation of the dynamic contact angle in liquid–liquid systems. *J. Colloid Interface Sci.* **146**, 226–241.
- GAO, P. & FENG, J. J. 2011a A numerical investigation of the propulsion of water walkers. *J. Fluid Mech.* **668**, 363–383.
- GAO, P. & FENG, J. J. 2011b Spreading and breakup of a compound drop on a partially wetting substrate. *J. Fluid Mech.* **682**, 415–433.
- GREENSPAN, H. P. 1978 On the motion of a small viscous droplet that wets a surface. *J. Fluid Mech.* **84**, 125–143.
- GURAU, V. & MANN JR., J. A. 2009 A critical overview of computational fluid dynamics multiphase models for proton exchange membrane fuel cells. *SIAM J. Appl. Maths* **70**, 410–454.



- HERDE, D., THIELE, U., HERMINGHAUS, S. & BRINKMANN, M. 2012 Driven large contact angle droplets on chemically heterogeneous substrates. *Europhys. Lett.* **100**, 16002.
- HERNÁNDEZ-SÁNCHEZ, J. F., LUBBERS, L. A., EDDI, A. & SNOEIJER, J. H. 2012 Symmetric and asymmetric coalescence of drops on a substrate. *Phys. Rev. Lett.* **109**, 184502.
- ITO, Y., HEYDARI, M., HASHIMOTO, A., KONNO, T., HIRASAWA, A., HORI, S., KURITA, K. & NAKAJIMA, A. 2007 The movement of a water droplet on a gradient surface prepared by photodegradation. *Langmuir* **23**, 1845–1850.
- KANG, Q., ZHANG, D. & CHEN, S. 2005 Displacement of a three-dimensional immiscible droplet in a duct. *J. Fluid Mech.* **545**, 41–66.
- KARPITSCHKA, S. & RIEGLER, H. 2012 Non-coalescence of sessile drops from different but miscible liquids: hydrodynamic analysis of the twin drop contour as a self-stabilizing traveling wave. *Phys. Rev. Lett.* **109**, 066103.
- KOIDO, T., FURUSAWA, T. & MORIYAMA, K. 2008 An approach to modeling two-phase transport in the gas diffusion layer of a proton exchange membrane fuel cell. *J. Power Sources* **175**, 127–136.
- LAI, Y.-H., HSU, M.-H. & YANG, J.-T. 2010 Enhanced mixing of droplets during coalescence on a surface with a wettability gradient. *Lab on a Chip* **10**, 3149–3156.
- MAGALETTI, F., PICANO, F., CHINAPPI, M., MARINO, L. & CASCIOLA, C. M. 2013 The sharp-interface limit of the Cahn–Hilliard/Navier–Stokes model for binary fluids. *J. Fluid Mech.* **714**, 95–126.
- MEHRABIAN, H. & FENG, J. J. 2011 Wicking flow through microchannels. *Phys. Fluids* **23**, 122108.
- MOGNETTI, B. M., KUSUMAATMAJA, H. & YEOMANS, J. M. 2010 Drop dynamics on hydrophobic and superhydrophobic surfaces. *Faraday Discuss.* **146**, 153–165.
- MOUMEN, N., SUBRAMANIAN, R. S. & MCLAUGHLIN, J. B. 2006 Experiments on the motion of drops on a horizontal solid surface due to a wettability gradient. *Langmuir* **22**, 2682–2690.
- NAM, J.-H., LEE, K.-J., HWANG, G.-S., KIM, C.-J. & KAVIANY, M. 2009 Microporous layer for water morphology control in PEMFC. *Intl J. Heat Mass Transfer* **52**, 2779–2791.
- NARHE, R. D., BEYSENS, D. A. & POMEAU, Y. 2008 Dynamic drying in the early-stage coalescence of droplets sitting on a plate. *Europhys. Lett.* **81**, 46002.
- OLAPADE, P. O., SINGH, R. K. & SARKAR, K. 2009 Pairwise interactions between deformable drops in free shear at finite inertia. *Phys. Fluids* **21**, 063302.
- RISTENPART, W. D., MCCALLA, P. M., ROY, R. V. & STONE, H. A. 2006 Coalescence of spreading droplets on a wettable substrate. *Phys. Rev. Lett.* **97**, 064501.
- SCHLEIZER, A. D. & BONNECAZE, R. T. 1999 Displacement of a two-dimensional immiscible droplet adhering to a wall in shear and pressure-driven flows. *J. Fluid Mech.* **383**, 29–54.
- SIBLEY, D. N., NOLD, A. & KALLIADASIS, S. 2013a Unifying binary fluid diffuse-interface models in the sharp-interface limit. *J. Fluid Mech.* **736**, 5–43.
- SIBLEY, D. N., NOLD, A., SAVVA, N. & KALLIADASIS, S. 2013b The contact line behaviour of solid–liquid–gas diffuse-interface models. *Phys. Fluids* **25**, 092111.
- SUBRAMANIAN, R. S., MOUMEN, N. & MCLAUGHLIN, J. B. 2005 Motion of a drop on a solid surface due to a wettability gradient. *Langmuir* **21**, 11844–11849.
- SUGIYAMA, K. & SBRAGAGLIA, M. 2008 Linear shear flow past a hemispherical droplet adhering to a solid surface. *J. Engng Maths* **62**, 35–50.
- WANG, C.-Y. 2004 Fundamental models for fuel cell engineering. *Chem. Rev.* **104**, 4727–4766.
- WANG, H., LIAO, Q., ZHU, X., LI, J. & TIAN, X. 2010 Experimental studies of liquid droplet coalescence on the gradient surface. *J. Supercond. Nov. Magn.* **23**, 1165–1168.
- WANG, X.-P. & WANG, Y.-G. 2007 The sharp interface limit of a phase field model for moving contact line problem. *Meth. Appl. Anal.* **14**, 287–294.
- XU, X. & QIAN, T. 2012 Droplet motion in one-component fluids on solid substrates with wettability gradients. *Phys. Rev. E* **85**, 051601.
- YUE, P. & FENG, J. J. 2011a Can diffuse-interface models quantitatively describe moving contact lines? *Eur. Phys. J., Spec. Top.* **197**, 37–46.
- YUE, P. & FENG, J. J. 2011b Wall energy relaxation in the Cahn–Hilliard model for moving contact lines. *Phys. Fluids* **23**, 012106.

- YUE, P., FENG, J. J., LIU, C. & SHEN, J. 2004 A diffuse-interface method for simulating two-phase flows of complex fluids. *J. Fluid Mech.* **515**, 293–317.
- YUE, P., FENG, J. J., LIU, C. & SHEN, J. 2005 Diffuse-interface simulations of drop coalescence and retraction in viscoelastic fluids. *J. Non-Newtonian Fluid Mech.* **129**, 163–176.
- YUE, P., ZHOU, C. & FENG, J. J. 2006a A computational study of the coalescence between a drop and an interface in Newtonian and viscoelastic fluids. *Phys. Fluids* **18**, 102102.
- YUE, P., ZHOU, C. & FENG, J. J. 2007 Spontaneous shrinkage of drops and mass conservation in phase-field simulations. *J. Comput. Phys.* **223**, 1–9.
- YUE, P., ZHOU, C. & FENG, J. J. 2010 Sharp-interface limit of the Cahn–Hilliard model for moving contact lines. *J. Fluid Mech.* **645**, 279–294.
- YUE, P., ZHOU, C., FENG, J. J., OLLIVIER-GOOCH, C. F. & HU, H. H. 2006b Phase-field simulations of interfacial dynamics in viscoelastic fluids using finite elements with adaptive meshing. *J. Comput. Phys.* **219**, 47–67.
- ZHANG, J., MIKISIS, M. J. & BANKOFF, S. G. 2006 Nonlinear dynamics of a two-dimensional viscous drop under shear flow. *Phys. Fluids* **18**, 072106.
- ZHOU, C., YUE, P., FENG, J. J., OLLIVIER-GOOCH, C. F. & HU, H. H. 2010 3D phase-field simulations of interfacial dynamics in Newtonian and viscoelastic fluids. *J. Comput. Phys.* **229**, 498–511.